Materials Research Express

PAPER • **OPEN ACCESS**

Microstructural properties and peritectic reactions in a binary Co–Sn alloy by means of scanning electron microscopy and atom probe tomography

To cite this article: Muna Khushaim *et al* 2020 *Mater. Res. Express* **7** 086508

Materials Research Express

OPEN ACCESS

RECEIVED
19 May 2020

REVISED
25 July 2020

ACCEPTED FOR PUBLICATION
6 August 2020

PUBLISHED
14 August 2020

PAPER

Microstructural properties and peritectic reactions in a binary Co–Sn alloy by means of scanning electron microscopy and atom probe tomography

Muna Khushaim[1,2], **Fatimah Alahmari**[3], **Nessrin Kattan**[1,2], **Delphine Chassaing**[4] **and Torben Boll**[4,5]

[1] Department of Physics, Faculty of Science, Taibah University, P. Box: 30002, P. Code 41447, Al-Madina, Saudi Arabia
[2] Nanotechonolgy Center, Taibah University, P. Box: 30002, P. Code 41447, Al-Madina, Saudi Arabia
[3] Department of Nanomedicine Research, Institute for Research and Medical Consultations (IRMC), Imam Abdulrahman bin Faisal University, Dammam 31441, Saudi Arabia
[4] Institute for Applied Materials (IAM-WK), Karlsruhe Institute of Technology (KIT), Hermann-von-Helmholtz-Platz 1, D-76344 Eggenstein-Leopoldshafen, Germany
[5] Karlsruhe Nano Micro Facility (KNMF), Karlsruhe Institute of Technology (KIT), Hermann-von-Helmholtz-Platz 1, D-76344 Eggenstein-Leopoldshafen, Germany

E-mail: Muna.Khushaim@gmail.com **and** mkhushaim@taibahu.edu.sa

Keywords: Co–Sn alloy, peritectic reactions, phase transformation

Abstract

Recent studies of lithium-ion batteries suggest that the use of binary CoSn alloys as anodes should provide an improvement over currently used anode materials. However, the implementation of CoSn alloys is challenging due to uncertainties regarding the phase transformations within this system. In order to understand these, we evaluate the compositions of different intermetallic compounds produced via the peritectic reactions, nucleate and grow within the microstructure of binary Sn − 25 at.% Co by employing atom probe tomography (APT). The stoichiometric CoSn phase, which is produced upon the cooling of the melt, is not only found as part of the peritectic solidification sequence but also as clusters within the pure *Sn* phase. The $CoSn_2$ phase was found as a nano sized layer and is attributed to the peritectic reaction between the CoSn phase and the pure *Sn* phase. The production of the $CoSn_3$ compound was enhanced by the phase transformation of the $CoSn_2$ phase. Furthermore, $CoSn_3$ clusters had formed in the pure *Sn* phase. A limited solubility within the pure Sn phase was also determined to be (0.6 ± 0.1) at.% Co.

1. Introduction

In comparison to currently used anodes in lithium ion batteries, especially carbonaceous materials, intermetallics promise higher energy densities in combination with relatively safe lithiation and delithiation voltages. Specifically, *Sn*-based alloys have been used in many different applications such as solder bumps [1], joining materials [2], and galvanizing technologies [3]. However, their most attractive application related to lithium ion batteries would be as electrodes [4–6], due to the 2.5 times higher theoretical capacity of batteries with Sn electrodes in comparison to graphite (372 mAh g^{-1} for graphite and 994 mAh g^{-1} for Sn) [7]. This led to Sn-based alloys being considered as an alternative material for anodes, especially in a nanostructured form [8]. However, the pure Sn electrode has not been put to practical use due to its poor cyclability and drastic volume change during Li insertion and extraction reactions [9]. To overcome these difficulties, the introduction of binary alloys has been proposed [10, 11]. Alloying Sn with other elements such as Cu, Co, Ni, and *V* or Fe and control of the particle size drastically changed the batteries' electrochemical behaviour. Co atoms, for example, can increase the stability of Sn-based electrodes [12]. The Co–Sn system has recently drawn increasing attention due to its special features such as amorphous Co–Sn particles, obtained by electrodeposition on a rough Cu foil [13], and nano CoSn crystals with different crystallite size [12]. These features improve the electrochemical behaviour of the CoSn material and that make it an attractive alternative for different industrial applications.

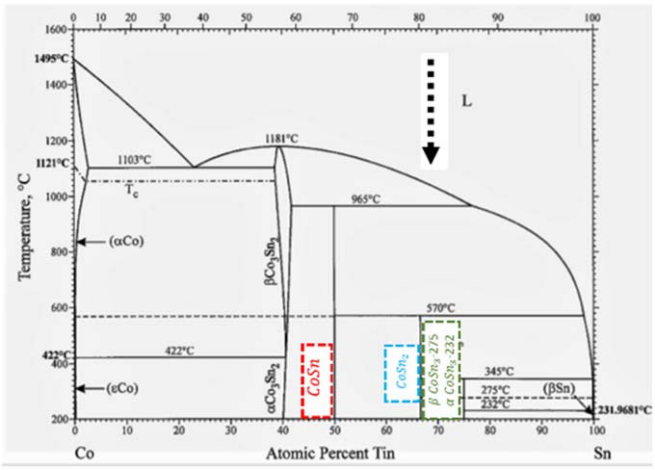

Figure 1. Binary Co–Sn phase diagram illustrated the Intermetallic phases. The figure reproduced from the [24].

However, the nature of the microstructure of the Co–Sn alloy plays an important role in its capability and functionality for many applications. Both crystalline CoSn compounds and crystalline alloys have been studied as electrode-active materials for lithium-ion batteries [14, 15]. Moreover, the electrochemical behaviours of an electrode consisting of Sn–Co amorphous particles have been investigated [16]. The improvements in the electrochemical reaction with the lithium differs between nanocrystalline and micron-sized CoSn compounds [12]. For example, the electrochemical behaviour of nanosized CoSn compound is very sensitive to the crystallite size, while for the microsized CoSn, the electrochemical reaction with lithium is limited to the insertion of a small amount of lithium. To control the microstructure and size of different intermetallic CoSn compounds, a study of the different reactions between different intermetallic phases exciting in the microstructure is important. Hence, a reliable thermodynamic description and analyses of different peritectic reactions that produce varying intermetallic phases within this system are critical. Different experimental studies investigated the Co–Sn phase diagram [17–19], and the thermodynamic properties of such systems in great detail have been reported [20, 21]. The crystalline phases observed in Co–Sn binary alloys are (a) the thermal solid solution of α Co and ε Co in Co-*rich* regions and (b) β Sn in Sn-rich corners. There are also different intermetallic compounds found such as CoSn, $CoSn_2$, β $CoSn_3$, and α $CoSn_3$ in *Sn*-rich corners [22, 23]. These phases are illustrated in a binary Co–Sn phase diagram in figure 1 [24]. These findings were heavily debated, with the binary Co–Sn phase diagram having changed significantly in the last decade. This is mainly due to the findings of $CoSn_3$ compounds [25–28]. Different melting temperatures and eutectic points of the observed intermetallic compounds within this system were also reported [29]. Those discrepancies can be explained by the experimental difficulties due to the high diffusivity of the Co atoms in the Sn matrix [30]. To overcome these different difficulties and to clarify the fundamental thermodynamic features in the Co–Sn system, solid-solid phase transformations of the different intermetallic compounds within this system should be investigated. The solid-state reactive diffusion effect in the Co–Sn system and the mechanism of the peritectic reactions between the pure Sn phase and other intermetallic Co–Sn compounds, are of great interest. Thus, a study of such reactions for different intermetallic compounds at the nanoscale is important to control the size of these compounds. To date, the morphologies and phase structural change of Sn-based anodes have been studied using *in situ* x-ray diffraction (XRD) and Mossbauer spectroscopy. In such studies, a combination of XRD with Mossbauer spectroscopy was used to probe the structural properties, mainly when the material consists of a small-scale nanocrystalline structure that is not confirmed using XRD [31, 32]. Moreover, the characterization of cycled Sn-based alloys was conducted with x-ray photoelectron spectroscopy (XPS) [33–36]. In another investigation by Ota *et al* time-of-flight secondary ion mass spectrometry (SIMS) was used to obtain information about the distribution of chemical species in a Co–Sn alloy used as an anode in a lithium-battery [37]. To the best of our knowledge, no studies have yet been performed to investigate the peritectic reactions and the phase transformations at the nano scale within this alloy. Knowledge about the peritectic reactions will help to understand the interfacial reactions between different phases, and their growth mechanism. Such a knowledge is important to control the sizes of the produced intermetallic compounds, and thus improve the electrochemical behaviour of CoSn alloy as anode material.

The objective of this study is to investigate the peritectic reactions within the binary Co–Sn alloy to understand the phase transformation between different intermetallic phases which are; CoSn, $CoSn_2$, $CoSn_3$, and pure Sn phase at atomic scale. These intermetallic compounds, which contain Sn, have been discussed

extensively as anode materials to provide efficient Li storage [12, 38]. Therefore, in the presented study, atom probe tomography (APT) in accompany with scanning electron microscopy (SEM) is applied to obtain quantitative information with nanometer resolution of the microstructure of a binary Co–Sn alloy with a composition of Sn- 25 at.% Co. APT analyses shed light on the phase transformations between the different intermetallic Co–Sn phases existing in the microstructure and will provide critical knowledge of the nano scale evaluation of the compositions for different reactions products, while the SEM images enhance the knowledge about the peritectic reactions that produce these products. APT produces three-dimensional quantitative chemical information with resolution better than one nanometer and allows us to quantify the gradient in concentration through each observed phase and the interfaces between different phases. This will help to investigate the phase transition behaviour of different Co–Sn intermetallic compounds. Moreover, using APT allows to investigate the local structure of the solid solution especially for the presence of clusters and nanoscale intermetallic phases. Such knowledge, cannot be achieved by SEM/EDX. The obtained results will truly play an important role in the further technical development of the investigated alloy.

2. Experimental

Appropriate quantities of Sn shots with a purity of 99.9% and Co shots with a purity of 99.9% were purchased from Sigma Aldrich and mixed at a ratio of 1:3: Co:Sn and subsequently melted in an arc melting furnace (Edmund Buhler GmbH) within a copper hearth. The sample was turned over and melted several times to completely homogenize the alloy composition. The arc-melting procedure was done in a chamber pumped to 1×10^{-3} *Pa* and backfilled with Ar gas to atmospheric pressure. The as synthesized alloys have been investigated by different characterization techniques.

XRD patterns of the powder samples were obtained using an x-ray diffractometer (STOE STADI MP), equipped with a Mythen 1 K silicon detector and a Cu anode producing mainly $Cu\ K\alpha_1$ radiation. The powder diffraction data were collected over a range from 10° to 90° in order to identify the intermetallic compounds in the microstructure of the prepared alloy. The samples were ground with a gate mortar beforehand.

The original microstructure morphologies were—without prior etching of the sample surface- investigated via SEM (Quanta 600) and x-ray spectroscopy (EDX). The samples were prepared by mounting a piece of the sample in a goniometer holder and mechanically grinding with *SiC* paper with 800 and 1200 grit size, respectively with distilled water. This step was followed by a final polishing using colloidal silica with a particle size of 30–120 nm on a cloth to eliminate scratches. The SEM micrographs were recorded at an accelerating voltage of 30 kV using a backscattered electron detector (BSE) to reveal the compositional contrast. Chemical analysis and elemental compositions were obtained with the EDAX system (EDS Inc., Mahwah, NJ, USA) from FEI. The chemical composition for each observed phase was estimated by averaging five measurements taken at different locations in the phase, while the errors were quantified by calculating the standard deviation for the obtained values of the chemical compositions.

Thermal analyses were performed using differential scanning calorimetry (DSC) in a Netzsch DSC 204 F1. The samples were placed in an Al_2O crucible and heated at heating rates of 5, 10, 15, 20, 25, and 30 K min^{-1}, respectively, under a dynamic nitrogen atmosphere (20 ml min^{-1}). The DCS signals were recorded while heating the alloy in the temperature range from 25 °C–800 °C.

APT required the preparation of needle-shaped samples using the focused ion beam (FIB) method. The FIB-based site-specific specimen preparation was performed with a FEI Zeiss Auriga 60 crossbeam system. The preparation of the APT tips in this study was done using the standard lift-out method [39] from the different specimen regions. Similarly, to FIB preparation for transmission electron microscopy (TEM), the area of interest, a phase boundary between the different intermetallic compounds in our case, was covered by *Pt* deposition. Then a lamella containing this microstructural feature was cut out, lifted out using an Oxford Omniprobe 400 micromanipulator. Two different ways were used to attach the lifted-out lamella on the microtip. The first one consisted of attaching the lamella without applying any rotation procedure on the micromanipulator, while the second one involved the rotation of the micromanipulator to allow the phase boundary to appear approximately horizontal in the lamella. Pieces of this lamella were then attached on Cameca microtip flattop posts. The attached piece was then shaped into a needle using a FIB annular milling pattern. The final annular milling of the respective tips was performed with a 5 KV *Ga* beam to reduce the thickness of the damaged layer created by the 30 KV *Ga* beam.

The APT experiments were performed in a CAMECA LEAP 4000X HR system using the UV-laser pulse mode to achieve a reasonable yield. The analytical parameters were chosen by performing different test analyses. It was found that 50 pJ for the laser energy and 25 K for the base analysis temperature offered a good compromise; minimizing local magnification effects while retaining a reasonable yield. The data were acquired at an average detection rate of 0.002–0.005 ions per pulse. The base pressure was maintained at less than 10^{-8} Pa

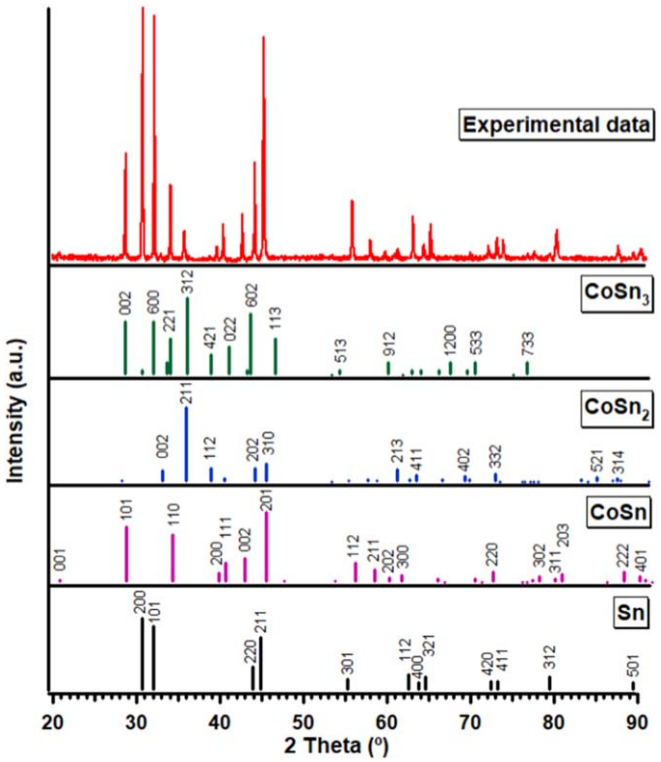

Figure 2. X-ray pattern for the prepared alloy, and expected peaks for *CoSn*, $CoSn_2$, $CoSn_3$ *and Sn phases*.

during the analysis. Reconstruction of the acquired data was performed using the software IVAS 3.6.14 provided by CAMECA. This reconstruction was calibrated based on the initial tip curvature radius measured via SEM. To quantify the chemical compositions within the different intermetallic phases and at the interfaces between them, the concentration profile along the *z*-axis of the cylinder within the whole volume of analysis was calculated. A cluster identification algorithm implemented in IVAS 3.6.14 was also used to estimate the shape and composition within the observed clusters in the microstructure by using a maximum separation distance of 1.5 nm between Co atoms and a minimum of 40 Co atoms in each cluster The microstructural features were also identified by using isoconcentration surfaces which delineate the regions containing more than 76 at.% Sn. This surface was obtained by sampling the APT reconstruction with $1 \times 1 \times 1$ nm^3 voxels after applying a delocalization procedure [40] with smoothing parameters of 3 nm for the x- and y-coordinates and 1.5 nm for the z-coordinate.

3. Results

The XRD pattern of the synthesized Sn −25 at.% Co is shown in figure 2. Compared with the standard powder X-ray diffraction data for metal *Sn* and Co–Sn intermetallics, the XRD lines of the Sn −25 at.% Co powder can be indexed as CoSn, $CoSn_3$, $CoSn_2$, and Sn, respectively. The CoSn intermetallic phase has a hexagonal crystal structure with a space group of P6/mmm [41]. For the $CoSn_3$ intermetallic phase, the presence of two structures has been reported; the first is β $CoSn_3$, which is formed by a peritectic reaction at 345 °C, and the second is low-temperature α $CoSn_3$, which is stable at 275 °C [27]. The space group of the high-temperature β $CoSn_3$ is Cmca with an orthorhombic crystal structure, while the space group of the low-temperature α $CoSn_3$ is $I4_1/acd$ with a tetragonal crystal structure. The pure *Sn* phase has a space group of $I4_1/amd$ with a body-centered tetragonal crystal structure [42]. The crystal structure of $CoSn_2$ is also tetragonal with a space group of I4/mcm [43]. Distinguishing between the α $CoSn_3$ and β $CoSn_3$ phases was not possible from the XRD data in figure 2 alone due to the similarity of the XRD patterns of both phases. Usually, α $CoSn_3$ and β $CoSn_3$ phases are modeled as a single-phase as suggested by Jiang *et al* [22].

To obtain a clear image of the morphologies and compositions of the different intermetallic phases in the synthesized alloy, SEM micrograph was recorded using BSE signals and is shown in figure 3. This figure reveals the presence of different contrast areas, in particular very bright regions among differently shaded gray areas. The gray areas appear as stripes and well-defined compact shapes. According to the EDX analyses, the bright gray stripe-shaped areas have an average chemical composition of (52 ± 3) at.% *Sn* and (48 ± 3) at.% Co, that is, an

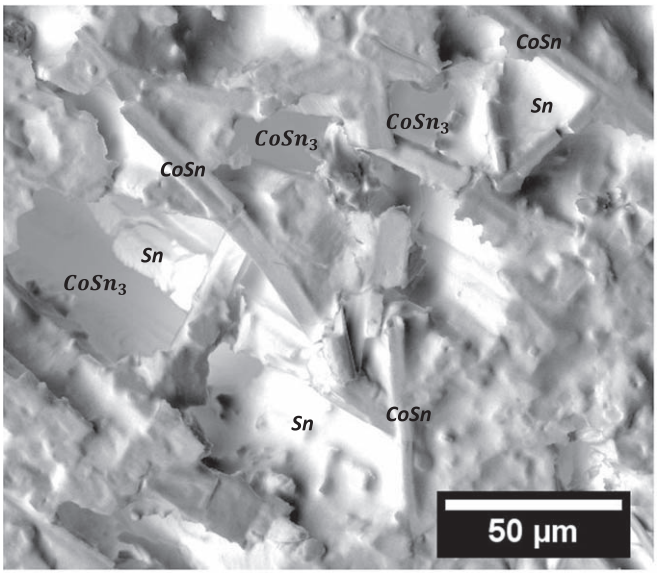

Figure 3. SEM micrograph of the Sn − 25%at. Co alloy reveals the presence of *CoSn*, *$CoSn_3$ and Sn phases* as measured by EDX.

approximate ratio of 1:1 Co:Sn, indicating that the stripe-shaped areas correspond to the *CoSn* phase. For the well-defined compact darker gray shapes, the EDX measurements quantified that the average chemical composition was (74.85 ± 0.9) at.% *Sn* and (25.14 ± 0.9) at.% Co, that is, an approximate ratio of 1:3 Co:Sn. This indicates that these crystals correspond to the *$CoSn_3$* phase. Moreover, the bright areas in this figure have an average composition of (99.4 ± 0.8) at.% Sn with a small fraction of Co atoms with a composition of (0.6 ± 0.1) at.% Co, indicating that those areas correspond to the pure Sn phase. In figure 3, the pure Sn phase was observed to be distinguishable from the two intermetallic phases, *CoSn* and *$CoSn_3$*. It should be noted that the Sn −25 at. % Co alloy was synthesized by arc-melting. This synthesizing procedure implies *Sn* metal acting as a flux to enhance the diffusion. Using the metal flux methodology usually reduces the activation energy barrier associated with solid-solid reactions and enhances the diffusion of the reactants in solid-state synthesis [44]. In this case, the liquid metal, Sn, acts not only as a solvent but also as a reactant providing species that can be incorporated into the final product. Inspection of the *Co–Sn* binary phase diagram in figure 1 reveals that during the cooling of the *Co–Sn* melt, with a composition of 1:3 *Co:* Sn, the solidification should occur at 965 °C under equilibrium cooling condition. On further cooling, the compound *CoSn* will crystallize until a temperature of 570 °C is reached. At this temperature, the solid *CoSn* will get involved in a peritectic reaction with the liquid *Sn*-rich melt to form *$CoSn_2$*. This phase envelopes the *CoSn* phase, which means that the peritectic reaction requires the diffusion of *Sn* through the enveloping *$CoSn_2$* phase. This process of diffusion usually takes a long time and will not finish before reaching the next peritectic equilibrium temperature of 345 °C. At this temperature, the β *$CoSn_3$* phase forms. In the end, the remaining melt will solidify at the eutectic temperature of 232 °C, and thus surround all of the formerly formed phases. Moreover, a single-phase sample of *$CoSn_3$* could also be obtained from the solidification of the melt with a composition of 1:3 *Co: Sn* and annealed for a very long time. In this case, the formed phase can be β *$CoSn_3$* if the annealing temperature is above 275 °C, or alternatively, it could be α *$CoSn_3$* at an annealing temperature of 275 °C or below [44]. The transformations of β *$CoSn_3$* into α *$CoSn_3$* was observed to occur slowly at annealing temperatures between 150 °C–200 °C, and the crystals of β *$CoSn_3$* phase was observed to remain for a long period of time during the annealing procedure and to grow together with the α *$CoSn_3$* phase [45]. However, in the tested alloy in this study, the use of large excess of *Sn* leads to crystals of *$CoSn_3$* and *CoSn* being embedded within the *Sn* rich matrix.

To discover the reactions behind the formation of these observed intermetallic phases and determine the temperature range at which they are stable, DSC analyses were performed. Figure 4 shows the DSC signals of the synthesized Sn −25 at.% *Co* alloy for different heating rates of 5, 10, 15, 20, 25, and 30 K min^{-1}. The DSC traces are almost identical for all of the heating rates with a small shift towards higher temperatures for faster heating rates as expected due to the difference in the reaction kinetics. The DSC signals can be interpreted as an exothermic reaction in the range of 200 °C–250 °C followed by an endothermic peak in the range of 250 °C–300 °C. There are also two exothermic peaks at approximately 350 °C and 580 °C. Comparison with the binary Co–Sn phase diagram in figure 1 implies that the exothermic peak in the range of 200 °C–250 °C might be correspond to the crystallization of the α *$CoSn_3$* phase. This is followed by the transition of the α *$CoSn_3$* to β *$CoSn_3$*, which manifests as the endothermic peak in the range of 250 °C–300 °C, knowing that the transition

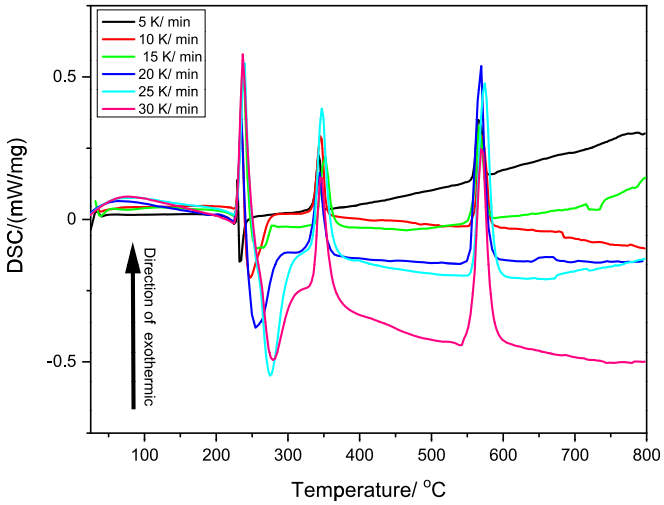

Figure 4. DSC signal of the Sn − 25%at. Co alloy for different heating rates.

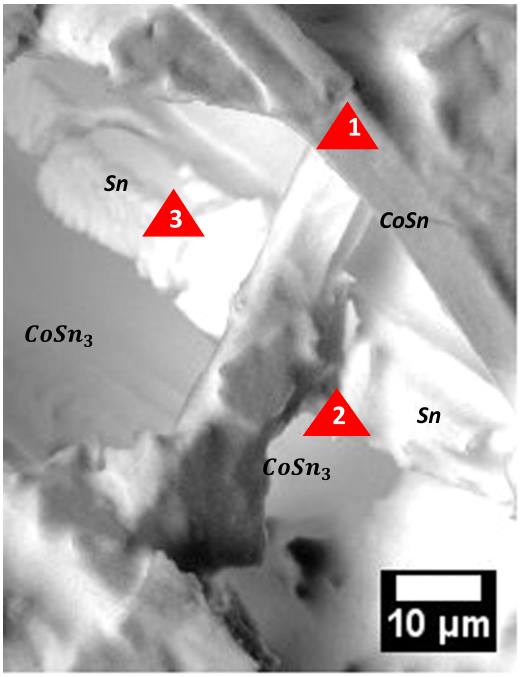

Figure 5. SEM micrograph indicating regions lifted out for the fabrication of APT tips.

temperature was reported at (275 ± 5) °C [22]. An exothermic crystallization peak observed at 350 °C indicates to the crystallization of new β $CoSn_3$ compounds. Finally, the exothermic signal at 580 °C stems from the crystallization of extra *CoSn* phase. The presented DSC signals are in the same range of the basic assessment of the DSC signals obtained by Jiang *et al* of this binary alloy [22] and also agrees with the SEM micrograph in figure 3. From literature, we expected the formation enthalpy of *CoSn* at 759 °C to be (−22 ± 0.4) KJ mol^{-1} and the formation enthalpy of β $CoSn_3$ at 331 °C to be (−13 ± 0.4) KJ mol^{-1} [46].

Considering the importance of the phase transformations between different intermetallic compounds and the involved peritectic reactions, an investigation using more advanced analytical techniques was needed. Thus, APT analyses were performed to obtain three-dimensional quantitative chemical information at a sub-nanometer resolution and thus allowed a detailed investigation for the alloy's microstructure, and then for the phase transformation at atomic scale. Figure 5 shows the magnified SEM micrograph of the alloy's microstructure, with the red triangles indicating the regions lifted out for the APT analyses. The sample microtips were lifted out from the *CoSn* phase region (triangle 1), near to the $CoSn_3/Sn$ interface (triangle 2) and

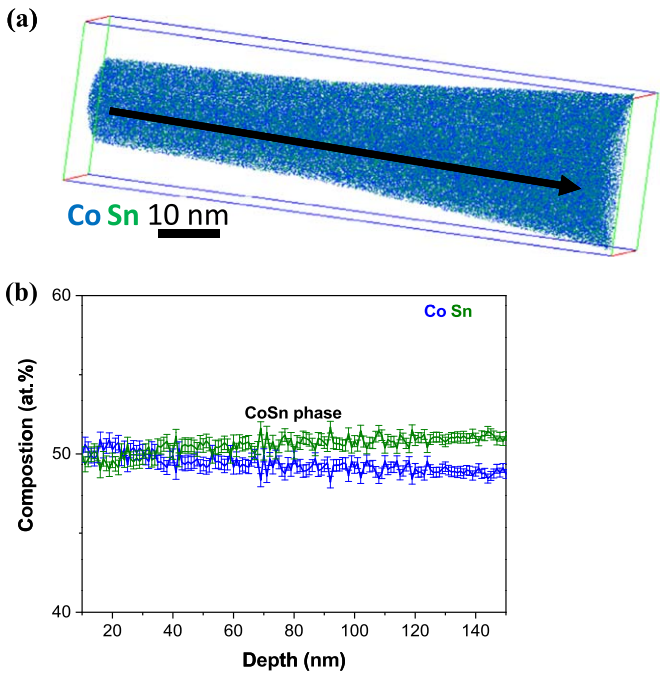

Figure 6. APT analysis of the sample microtip lifted out from the *CoSn* phase region (triangle 1 in figure 5). (a) The reconstructed volume. (b) A concentration profile with step size of 0.1 nm for the whole volume along the tip axis indicated by the black arrow in (a).

from *Sn* phase region (triangle 3). The prepared microtips with an apex radius in the range of 50 nm were then obtained.

Several APT measurements were performed on the microtips fabricated from the region indicated by triangle (1) in figure 5. One reconstruction of these measurements is shown in figure 6. The reconstructed volume containing 4 million atoms is shown in figure 6(a). The data quality was assessed by observing the desorption map, confirming good homogeneity of the hit density during the APT analysis. One difficulty encountered in this APT analysis is to distinguish ions with the same mass to charge ratio (m/q). Co^{+} and Sn^{++} peaks overlap at a m/q ratio value of 59 *a.m.u*. To overcome this difficulty, a peak deconvolution algorithm provided by IVAS 3.6.14 was used to deconvolute the peaks, assuming a natural isotopic abundance for Sn and *Co*. A concentration profile with step size 0.1 nm for the whole volume along the tip axis as indicated by the black arrow in figure 6(a) is presented in figure 6(b). The whole reconstructed volume consists of one homogenous phase with a composition of (50.6 $\pm$ 0.4) at.% Sn and (49.3 $\pm$ 0.4) at.% *Co*. We therefore identify the whole volume of analysis in figure 6(a) as a homogenous CoSn phase. This composition is in almost perfect agreement with the CoSn composition as detected by an EDX analysis in figure 3. Moreover, the obtained compositions for the CoSn phase from both APT and EDX agree well with the expected composition from the binary Co–Sn phase diagram (figure 1).

The next APT analysis traced the local chemistry at the atomic scale in the region containing the $CoSn_3$/Sn interface (indicated by triangle (2) in figure 5). APT measurements performed for the fabricated microtips from this lifted out lamella yielded two large data sets with 36 million atoms and 42 million atoms. The reconstructed volumes for these two measurements are shown in figures 7 and 8, respectively. The 3D- elemental map of Co and Sn atoms for the analyzed microtip that yielded 36 million atoms in figure 7(a) reveals the presence of the two-phase regions. To identify these phases, the concentration profile with step size of 0.1 nm within the cylinder aligned along the tip axis, as indicated by the black arrow in figure 7(a), was calculated and presented in figure 7(b). The composition at the upper part of the reconstructed volume (named as phase 1) corresponds to (97.9 $\pm$ 0.04) at.% Sn and (0.6 $\pm$ 0.01) at.% Co, with a small amount of contaminations by *Pt* and *Ga* from the preparation procedure. The amounts of *Ga* and *Pt* impurities in the whole volume of analysis were estimated to be around (1 $\pm$ 0.01) at.% for *Pt* and (0.5 $\pm$ 0.01) at.% *Ga*. Inspection of the concentration profile in figure 7(b) reveals that the composition at the lower part of the reconstructed volume (named as phase 2) corresponds to (69.6 $\pm$ 0.2) at.% *Sn* and (29.4 $\pm$ 0.2) at.% *Co*. *Pt* impurities with composition of (3 $\pm$ 0.01) at.% were observed also at this part of the reconstructed volume. According to these measured compositions, the observed phases regions can be identified as follows: phase 1 corresponds to the pure Sn phase with a limited solubility of *Co* atoms (0.6 $\pm$ 0.01) at.%, while for phase 2, the composition value has a ratio of Sn/Co $\approx$ 2.3. This ratio almost matches stoichiometric $CoSn_2$. The slight deviation from the expected stoichiometric $CoSn_2$ phase,

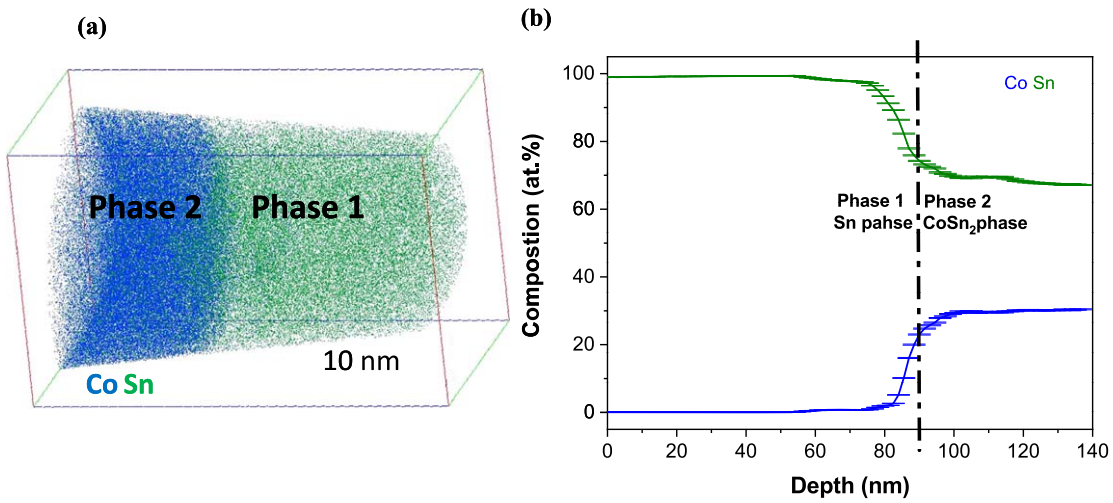

Figure 7. First APT analysis of the sample microtip lifted up in the $CoSn_3/Sn$ interface (triangle 2 in figure 5). (a) The reconstructed volume of analysis with the two phases regions. (b) A concentration profile with step size of 0.1 nm along the *z*-axis of a cylinder placed perpendicular to the interphase interface.

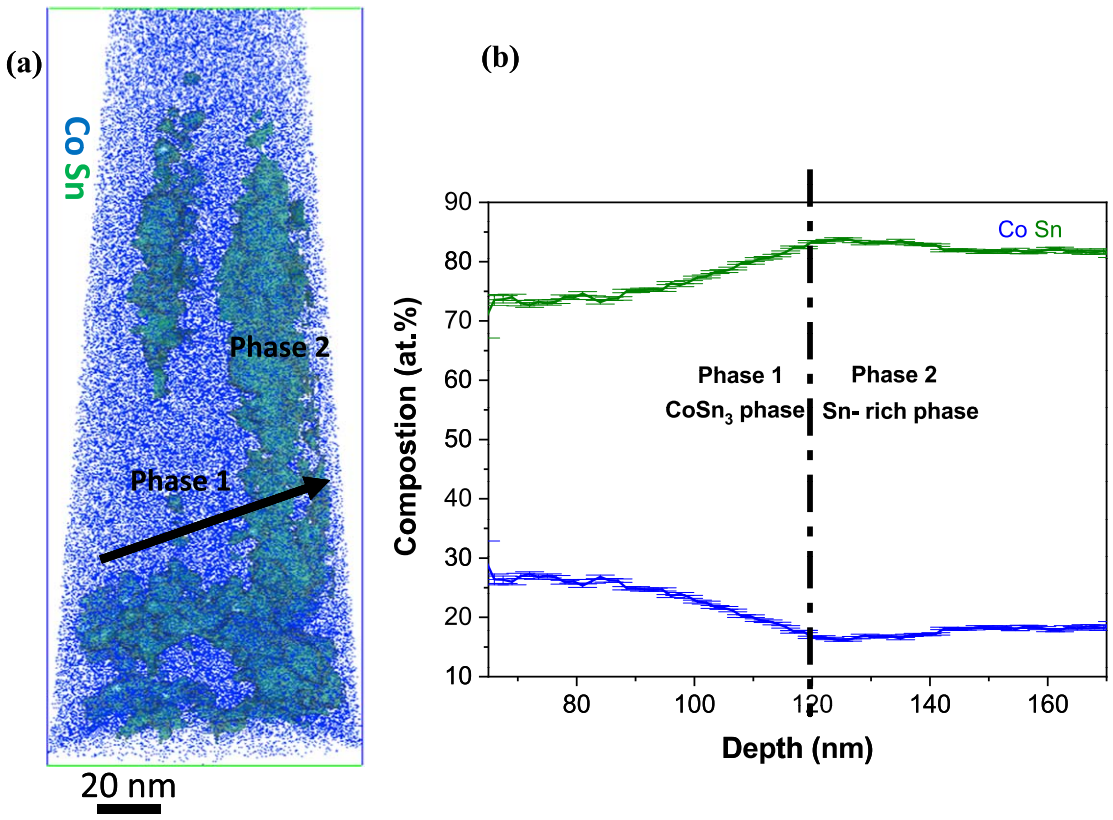

Figure 8. Second APT analysis of the sample microtip lifted up in the $CoSn_3/Sn$ interface (triangle 2 in figure 5). (a) The reconstructed volume of analysis with the isoconcentration surface delineates the regions containing more than 76 at.% Sn. (b) A concentration profile along the cylinder aligned as indicated by black arrow in (a).

which is Sn/Co ≈ 2, might be attributed to the presence of *Pt* impurities, which cannot be easily explained as contamination stemming from FIB preparation. Despite this, it can be concluded that the phase 2 in figure 7(b) corresponds to $CoSn_2$.

3D- elemental map of Co and Sn atoms for the analyzed microtip that yielded 42 million atoms is shown in figure 8(a). Several linear composition profiles along x, y and z axes were obtained. However, the gradient in the composition within the reconstructed volume was observed along x and y axes. This observation was confirmed by applying an isoconcentration surface delineates the regions containing more than 76 at.% Sn as shown in

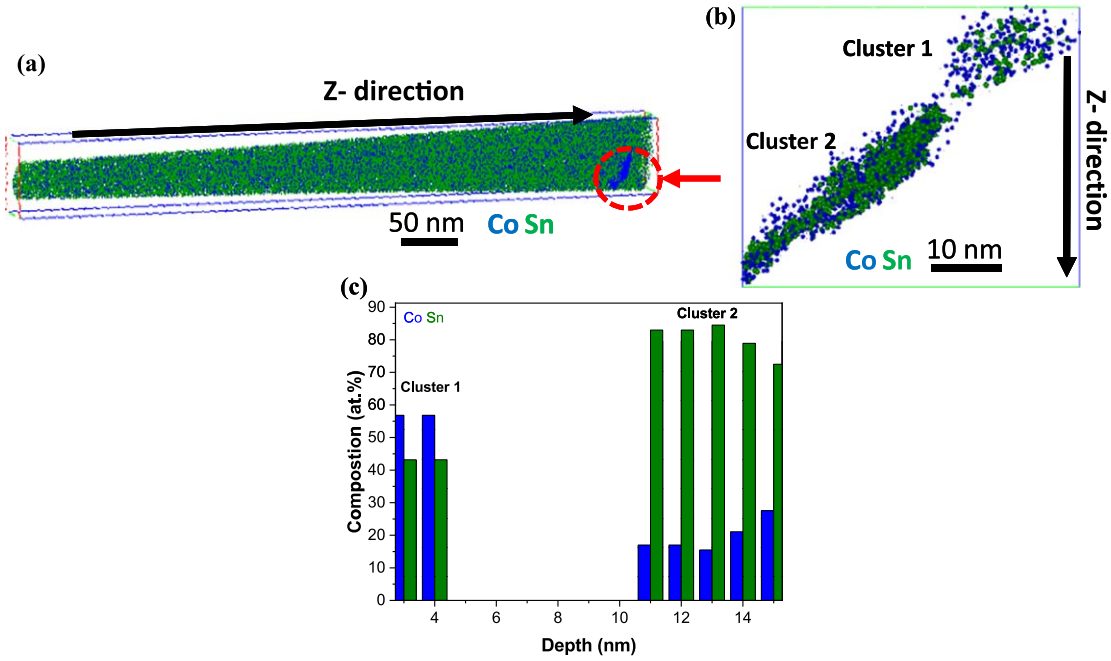

Figure 9. APT analysis of the sample microtip lifted up in the *Sn* phase region. (a) The reconstructed volume of analysis showing the accumulation of Co atoms as indicated by the red circle and arrow (z-direction has been identified by black arrow) (b) A clipped part from the bottom of the analyzed volume showing the distribution of Co and Sn atoms within the observed two clusters (z-direction has been identified by black arrow) (c) concentration profile obtained for cluster 1 and cluster 2 in (b) along the z direction.

figure 8(a). Thus, identification of the composition gradient was done by obtaining the concentration profile along the cylinder aligned as indicated by the black arrow in figure 8(a). This concentration profile is shown in figure 8(b) and reveals the presence of (75.24 $\pm$ 0.4) at.% *Sn* and (24.73 $\pm$ 0.4) at.% *Co* at the left region of the reconstructed volume (named as phase 1 in figure 8), while the right region of this volume consists of (82.18 $\pm$ 0.1) at.% Sn and (17.8 $\pm$ 0.1) at.% Co (named as phase 2 in figure 8). The presence of a homogenous compound along x and y axes that consists of Sn and Co with a ratio of Sn/Co $\approx$ 3 gives a strong hint to the presence of an intermetallic $CoSn_3$ phase in this measurement. However, along z direction, the dataset shows a mostly homogenous composition along the whole volume of analysis with the values of (85.2 $\pm$ 0.1) at.% Sn and (14.8 $\pm$ 0.1) at.% *Co*. A preferential magnification or a local magnification effect with element specific trajectory deviations could, as an APT artefact, also produce deviating compositions along crystallographic directions. In a mono-crystalline sample, these regions would be columns located at some (not all) lower indexed poles, as observed by different groups for intermetallics [47–49]. Neither the concentration in this measurement nor in any other measurement did show this behaviour. Thus, we conclude the observation in figure 8 to be evidence for the presence of a different phase. Moving out from the area of the $CoSn_3$ phase, the graph shows a Sn enriched region with a ratio of Sn/Co $\approx$ 4.6, according to concentration profile in figure 8(b). One explanation for this finding is that indeed the Sn rich region contains extremely small clusters of another phase or, more likely, that the phase interface is extremely rough, meaning the right side of the graph is the mix of two different phases for either option.

The final APT analysis, in this study, was performed for the pure *Sn* phase region prepared from the lifted-up region indicated by triangle (3) in figure 5. The tip's reconstructed volume in figure 9(a) consists of more than 70 million atoms. After obtaining the concentration profile for the whole reconstructed volume along the tip axis, it was found that this volume consists of (99.34 $\pm$ 0.008) at.% Sn and (0.65 $\pm$ 0.008) at.% Co. This calculated value of the chemical composition is nearly the same as the one obtained for the phase 1, that is the pure Sn phase, observed in figure 7(a). A Co rich cluster was observed in the pure Sn phase and indicated by the red circle and arrow in figure 9(a). *Co* accumulated clusters of about 10–20 nm are visible. The cluster identification algorithm from IVAS 3.6.14 allowed us to identify Co-containing clusters using a maximum separation distance of 1.5 nm between Co atoms and a minimum of 40 Co atoms in each cluster, which we identified as good parameters choice from nearest neighbour analysis with an interatomic separation of 4 nm in the immediate vicinity around Co atoms. The distribution of Co and Sn atoms was detected within these clusters as shown in the cluster's distribution in the reconstructed volume's clip part in figure 9(b). This figure reveals two separate clusters, which are in close vicinity to but not in direct contact with each other, named as cluster 1 and cluster 2. The concentration profile obtained for these clusters is shown in figure 9(c). According to this figure, the average

composition of cluster 1 was found to be (45.9 ± 0.5) at.% *Sn* and (54.1 ± 0.1) at.% Co, with a ratio of Sn/Co ≈ 1, while the cluster 2 has an average composition ratio of (76.65 ± 0.5) at.% Sn and (23.34 ± 0.3) at.% Co, with a ratio of $Sn/Co \approx 3.2$.

4. Discussion

Inspection of the Co–Sn binary phase diagram in figure 1 with special attention to the *Sn*-rich portion reveals the presence of two phases of $CoSn_3$, which are α and β. Moreover, other phases can be observed in the diagram around the composition of 1:3 Co:Sn. These phases are the CoSn and $CoSn_2$. The reaction responsible for producing the $\beta CoSn_3$ is [22]:

$$L\ (Sn\ rich\ melt) + CoSn_2 \rightarrow \beta\ CoSn_3 \quad (1)$$

This reaction happened at 345 °C. However, the transition of $\beta CoSn_3$ to α $CoSn_3$ take place at 275 °C. For the reaction path related to the CoSn and $CoSn_2$ phases, it is written as a peritectic reaction of [50]:

$$CoSn + L(Sn\ rich\ melt) \rightarrow CoSn_2 \quad (2)$$

Reaction (2) usually occurs at 570 °C. Finally, the production of the CoSn phase take place during the cooling of the liquid Co–Sn with a composition of 1:3. At 965 °C, this reaction is [43]:

$$L(with\ 1{:}\ 3;\ Co{:}\ Sn) \rightarrow CoSn + L(Sn\ rich\ melt) \quad (3)$$

While the DSC signals (figure 4) are useful for observing the phase transformations of the different crystalline phases, this technique does not explain the peritectic reactions involved in equations (1)–(3). A combination of the SEM micrograph in figure 3 with the APT measurements in figures 6–9 confirms the aforementioned reactions. While it was not possible to investigate the crystal structure, as done for example by Boll *et al* [48, 49], in the observed intermetallic compounds due to the measurements requiring the laser mode, the compositional analysis still allowed the identification of composition of the respective phases. The APT measurements in this study confirm the presence of the *CoSn* (figure 6), the $CoSn_2$ (figure 7), the $CoSn_3$ (figure 8) and the pure Sn (figures 7 and 9) phases. The occurrence of all equilibrium phases in the microstructure of the prepared alloy corroborates the agreement with the binary Co–Sn phase diagram (figure 1). The proceeding of peritectic reactions described in equations (1) and (2) was achieved by using *Sn* as a reactive flux. During the preparation of our tested alloy, which has a composition ratio of 1:3 Co:Sn, a rapid cooling of the melt was achieved after the arc-melting. Thus, crystals of CoSn were obtained as shown in SEM micrograph in figure 3. According to the APT measurement for this phase in figure 6, the CoSn has a nearly exact stoichiometric composition of 1:1 Co:Sn ratio, which is in good agreement with the binary Co–Sn phase diagram (figure 1). This indicates the presence of CoSn phase close to its equilibrium state.

Crystals of CoSn with a higher Co content than that of the Sn-rich matrix usually reacts with the pure Sn phase which was observed to envelope these CoSn crystals (figure 3). This peritectic reaction processed to produce the microcrystals of the $CoSn_2$ compound (according to equation (2)). In our case, the $CoSn_2$ phase was observed to nucleate directly in the *Sn*-rich matrix. Such observation is deduced from the sharp interface between the $CoSn_2$ and *Sn* phases (figure 7(b)). Moreover, the observed $CoSn_2$ phase was quite thin, only about ~60 nm in thickness, meaning it only exists as a nanoscale thin layer. This explains the lack of this phase observed by SEM in figure 3. This confirms a study by Wang *et al* [51] who noted the presence of an irregular shape of the thin $CoSn_2$ phase. One should find the presence of the $CoSn_2$ phase (named as phase 2) accompanying the pure *Sn* phase (named as phase 1) in figure 7. Thus, a peritectic reaction of the $CoSn_2$ layer with the pure *Sn* phase ((99.4 ± 0.01) at.% Sn) was expected according to equation (1) to produce the $CoSn_3$ phase. Thus, the driving force of the $CoSn_3$ formation from $CoSn_2$ phase induced a rapid phase transformation of $CoSn_2$ phase to $CoSn_3$ phase. One possible explanation of the driving force of this phase transformation is the difference in the Gibbs free energy between the single phase $CoSn_3$ and the two phases; *Sn* and $CoSn_2$ [51]. It was found that this difference in the Gibbs free energy increases with decreasing temperature, and thus at higher temperature, a weaker driving force for the phase transformation would be expected. As a result, the nucleation of the $CoSn_3$ phase becomes more difficult at higher temperature. Thus, the slower of kinetics reaction for the phase transformation would be expected resulting in the formation of small region or clusters of $CoSn_3$ phase (figure 9). Upon the complete transformation of the previously formed $CoSn_2$ into the $CoSn_3$ phase, the diffusion of *Sn* atoms across the $CoSn_3$ phase was enhanced by this complete transformation of the $CoSn_2$ layer, and hence enhancing the growth of the $CoSn_3$ crystals. These crystals can be observed clearly in SEM micrograph in figure 3. Moreover, APT analysis in figure 8 revealed the presence $CoSn_3$ phase surrounded by *Sn* rich area. This observation might indicate to the proceeding of the peritectic reaction that produces $CoSn_3$ crystal.

According to the phase diagram in figure 1, the remaining melt solidifies at the eutectic temperature of 229 °C, and was indeed observed to surround the formerly formed phases. The APT final analysis in figure 9 was performed in the pure *Sn* phase region. The limited solubility of Co atoms within the pure Sn phase was measured to be ~0.65 at.% Co. This value is in a good agreement with the obtained value by EDX measurement in figure 3. Moreover, nanometer scale Co clusters were observed in the microstructure of pure Sn phase. The measured compositions of the observed clusters revealed the presence of the ratios of Sn/Co ≈ 1 and Sn/Co ≈ 3.2 within these clusters. Inspection of the phase diagram in figure 1 reveals the reduction on Co solubility by lowering the temperature. Thus, different intermetallic phases will nucleate and form in the microstructure. The nucleation of Co clusters in the pure Sn phase in figure 9 is possible due to its limited solubility. In cluster 1, Co atoms cluster with Sn at nearly 1:1 Co: Sn ratio; in which its growth would be expected to form the CoSn phase (figures 3 and 6). However, the presence of cluster 1 may have deformed the surrounding matrix enough to produce nucleation sites for clusters of other phases causing the nucleation of the $CoSn_3$ (cluster 2). These observations explain the presence of the two exothermic peaks at 350 °C and 580 °C in figure 4, which corresponds to the crystallization of *CoSn* and $CoSn_3$ phases. The presences of *Co* clusters with (54.1 ± 0.1) at.% *Co* in cluster1, (23.34 ± 0.3) at.% Co in cluster 2 and the composition of (0.6 ± 0.1) at.% *Co* in pure Sn are consistent with the equilibrium phase diagram that indicates there is limited solubility of Co in Sn (up to 0.6%) at a temperature of 1196 °C [52].

This study presents a method to investigate the phase transition behaviour of different Co–Sn intermetallic compounds applying APT. Such knowledge is extremely important to understand the mechanism of the peritectic reactions that produce observed intermetallic Co–Sn compounds and subsequently demonstrate how to control the sizes and morphologies of these compounds. Additionally, it has been proven that the involved peritectic reaction implies the presence of different pre-crystallized clusters [53]. The APT technique has proven to be powerful for investigating the local structure of the solid solution and the assembly of clusters. This may lead to more detailed future research including the influence of additives such as Co–Sn alloy embedded carbon nanofiber (Co–Sn/CNF) composites [54] and the effect of the minor addition of Zn atoms to the binary Co–Sn system [55]. Probing the microstructure at nanoscale and revealing the distribution of different constitutional elements by using APT will truly facilitates the design and hence the improvement of such important alloy system.

5. Conclusion

A liquid Sn phase was utilized as a metal flux to prepare Sn −25 at.% Co alloy. Characterization of the synthesized alloy using XRD and SEM/EDX provided clear evidence of the well-defined crystalline nature of the microstructure. The existing intermetallic compounds were identified as CoSn (hexagonal crystal structure), $CoSn_2$ (tetragonal crystal structure), $CoSn_3$ (orthorhombic crystal structure for the β $CoSn_3$ and tetragonal crystal structure for the α $CoSn_3$), and pure *Sn* phases (body-centered tetragonal crystal structure). The temperature range at which the observed intermetallic phases were crystalized was determined using the DSC analysis. The result shows the phase crystallization temperatures of $CoSn_3$, CoSn phases are 350 °C and 580 °C, respectively. The peritectic reactions and the phase transformations products were analysed at varying locations in the respective alloy via SEM and APT. The series of phase transformations was started by the production of the stoichiometric compound CoSn which was nucleate and growth upon the cooling of the melt. This compound later react with the enriched Sn matrix to produce the nanosized layer of $CoSn_2$ phase. On the next step, the production of the $CoSn_3$ compound was enhanced by the phase transformation of $CoSn_2$ phase.

APT revealed *Co* clusters with (54.1 ± 0.1) at.% *Co* and (23.34 ± 0.3) at.% Co, where (0.6 ± 0.1) at.% *Co* was observed in pure Sn, which is consistent with the equilibrium phase diagram that indicates there is limited solubility of Co in Sn (up to 0.6%) at a temperature of 1196 °C. This limited solubility of Co atoms induced the formation of different observed intermetallic phases that are *CoSn* and $CoSn_3$. This study demonstrates the unique capabilities of APT to characterize a series of peritectic reactions within the binary Co–Sn alloy.

Acknowledgments

The authors would like acknowledge the Karlsruhe Nano Micro Facility (KNMF) of the Karlsruhe Institute of Technology for providing access to the instruments at their laboratories (KNMF proposal number 2017-018-019469) and the core lab facilities in King Abdullah University of Science and Technology (KAUST).

ORCID iDs

Muna Khushaim https://orcid.org/0000-0002-0941-7086
Nessrin Kattan https://orcid.org/0000-0002-6766-3517

References

[1] Labie R, Beyne E, Mertens R, Ratchev P and Humbeeck J V 2003 Investigation of the reliability of Cu and Co UBM layers in thermal-cycling tests *Proc. of the 5th Electronics Packaging Technology Conf. (EPTC 2003)* (https://doi.org/10.1109/EPTC.2003.1271588.)
[2] Liu L, Andersson C and Liu J 2004 Thermodynamic assessment of the Sn–Co lead-free solder system *J. Electron. Mater.* **33** 935–9
[3] Tomachuk C R, de C M, Freire A, Ballester M, Fratesi R and Roventi G 1999 Pulse electroplated ZnCo alloys *Surf. Coat. Technol.* **122** 6–9
[4] He J, Zhao H, Wang J, Wang J and Chen J 2010 Hydrothermal synthesis and electrochemical properties of nano-sized Co–Sn alloy anodes for lithium ion batteries *J. Alloys Compd.* **508** 629–35
[5] Jang B O, Park S H and Lee W J 2013 Electrospun Co–Sn alloy/carbon nanofibers composite anode for lithium ion batteries *J. Alloys Compd.* **574** 325–30
[6] Ui K, Kikuchi S, Yasuhiro J and Naoaki K 2011 Preparation of Co–Sn alloy film as negative electrode for lithium secondary batteries by pulse electrodeposition method *J. Power Sources* **196** 3916–20
[7] Wachtler M, Besenhard J O and Winter M 2001 Tin and tin-based intermetallics as new anode materials for lithium-ion cells *J. Power Sources* **94** 189–93
[8] Mulas G, Enzo S, Bonatto Minella C, Arca E, Gerbaldi C, Penazzi N, Bodoardo S, Hassoun J and Panero S 2009 Mechanochemical synthesis and electrochemical properties of nanostructured electrode materials for Li ion batteries *J. Solid State Electrochem.* **13** 239–43
[9] Winter M and Besenhard J O 1999 Electrochemical lithiation of tin and tin-based intermetallics and composites *Electrochim. Acta* **45** 31–50
[10] Lee H Y, Kim Y L, Hong M K and Lee S M 2005 Carbon-coated Ni20Si80 alloy–graphite composite as an anode material for lithium-ion batteries *J. Power Sources* **141** 159–62
[11] Lindsay M J, Wang G X and Liu H K 2003 Al-based anode materials for Li-ion batteries *J. Power Sources* **119–121** 84–7
[12] Alcántara R, Rodríguez I and Tirado J L 2008 Structural and electrochemical properties of micro- and nano-crystalline CoSn electrode materials *Chem. Phys. Chem.* **9** 1171–7
[13] Ferguson P P, Todd A D W and Dahn J R 2008 Comparison of mechanically alloyed and sputtered tin–cobalt–carbon as an anode material for lithium-ion batteries *Electrochem. Commun.* **10** 23–31
[14] Ionica-Bousquet C M, Lippens P E, Aldon L, Olivier-Fourcade J and Jumas J C 2006 *In situ* 119Sn Mössbauer effect study of Li−$CoSn_2$ electrochemical system *Chem. Mater.* **18** 6442–7
[15] Alcántara R, Ortiz G F and Tirado J L 2007 Unfolding tin–cobalt interactions in oxide-based composite electrodes for Li-ion batteries by Mössbauer spectroscopy *Chem. Phys. Chem.* **8** 80–6
[16] Kim J and Cho H 2007 Synthesis and morphological, electrochemical characterization of Sn92Co8 nanoalloys for anode materials in Li secondary batteries *J. Electrochem. Soc.* **154** A462–6
[17] Lewkonja K 1908 Metallographische Mitteilungen aus dem Institut für physikalische Chemie der Universität Göttingen *LXV. Über die Legierungen des Kobalts mit Zinn, Antimon, Blei, Wismut, Thallium, Zink, Cadmium, Chrom und Silicium. Zeitschrift für anorganische Chemie* **59** 293–345
[18] Żemczużny S F and Belynsky S W 1908 Kobalt-Zinnlegierungen *Zeitschrift für Anorganische Chemie* **59** 364–70
[19] Cömert H and Pratt J N 1992 Constitutional studies of cobalt-tin alloys *Metall. Trans.* A **23** 2401–7
[20] Predel B and Vogelbein W 1979 Bildungsenthalpien fester legierungen der binären systeme des eisens, kobalts und nickels mit germanium und zinn *Thermochim. Acta* **30** 201–15
[21] Torgersen A N, Bros H, Castanet R and Kjekshus A 2000 Enthalpy of formation for CoGe, CoSn, $Ni_{3.14}Sn_4$, $Ni_{3.50}Sn_4$, $AuCo_{1.66}Sn_4$, $AuNi_2Sn_4$ and $Au_{1.17}Pt_{1.82}Sn_4$ *J. Alloys Compd.* **307** 167–73
[22] Jiang M, Sato J, Ohnuma I, Kainuma R and Ishida K 2004 A thermodynamic assessment of the Co–Sn system *Calphad* **28** 213–20
[23] Massalski T B 1986 *Binary Alloy Phase Diagrams* (Metals Park: ASM) (https://doi.org/10.1002/adma.19910031215)
[24] Okamoto H 2006 Co–Sn (cobalt-tin) *Journal of Phase Equilibria and Diffusion* **27** 308
[25] Vassilev G P and Lilova K I 2006 Contribution to the thermodynamics of the Co–Sn system *Arch. Metall. Mater.* **51** 365–75 http://www.imim.pl/files/archiwum/Vol3_2006/art6.pdf
[26] Comert H and Pratt J N 1985 The thermodynamic properties of solid cobalt-tin alloys *Thermochim. Acta* **84** 273–86
[27] Lang A and Jeitschko W 1996 Two new phases in the system cobalt-tin: the crystal structures of α- and β-$CoSn_3$ *Z. Metallkd* **87** 759–64 https://inis.iaea.org/search/searchsinglerecord.aspx?recordsFor=SingleRecord&RN=28023025
[28] Okamoto H 2006 Co–Sn (cobalt-tin) *J. Phase Equilib. Diff* **27** 308–308
[29] Liu L, Li J F, Zhao S and Zhou Y H 2009 Redetermination of the eutectic composition of the Co–Sn binary alloy *Journal of Phase Equilibria and Diffusion* **30** 242–5
[30] Ortiz G F, Alcantara R, Rodriguez I and Tirado J L 2007 New tin-based materials containing cobalt and carbon for lithium-ion batteries *J. Electroanal. Chem.* **605** 98–108
[31] Connor P A and Irvine J T S 2002 Combined x-ray study of lithium (tin) cobalt oxide matrix negative electrodes for Li-ion batteries *Electrochim. Acta* **47** 2885–92
[32] Todd A D W, Dunlap R A and Dahn J R 2007 Mössbauer effect studies of sputter-deposited tin–cobalt and tin–cobalt–carbon alloys *J. Alloys Compd.* **443** 114–20
[33] Ehinon K K D, Naille S, Dedryvère R, Lippens P E, Jumas J C and Gonbeau D 2008 Ni_3Sn_4 electrodes for Li-ion batteries: Li−Sn alloying process and electrode/electrolyte interface phenomena *Chem. Mater.* **20** 5388–98
[34] Naille S, Dedryvère R, Martinez H, Leroy S, Lippens P E, Jumas J C and Gonbeau D 2007 XPS study of electrode/electrolyte interfaces of η-Cu_6Sn_5 electrodes in Li-ion batteries *J. Power Sources* **174** 1086–90
[35] Leroy S, Martinez H, Dedryvère R, Lemordant D and Gonbeau D D 2007 Influence of the lithium salt nature over the surface film formation on a graphite electrode in Li-ion batteries: an XPS study. *Appl. Surf. Sci.* **253** 4895–905

[36] Wang X, Hironaka T, Hayashi E, Yamada C, Naito H, Segami G, Sakiyama Y, Takahashi Y and Kibe K 2007 Electrode structure analysis and surface characterization for lithium-ion cells simulated low-earth-orbit satellite operation: II. Electrode surface characterization *J. Power Sources* **168** 484–92
[37] Ota H, Akai T, Namita H, Yamaguchi S and Nomura M 2003 XAFS and TOF–SIMS analysis of SEI layers on electrodes *J. Power Sources* **119–121** 567–71
[38] Guo H, Zhao H, Jia X, Li X and Weihua Q 2007 A novel micro-spherical $CoSn_2$/Sn alloy composite as high capacity anode materials for Li-ion rechargeable batteries *Electrochim. Acta* **52** 4853–7
[39] McKenzie W R, Marquis E A and Munroe P R 2010 Focused ion beam sample preparation for atom probe tomography *Microscopy: Science, Technology, Applications and Education* (Internet resource: ORMATEX RESEARCH CENTER.) 1800–10 http://handle.unsw.edu.au/1959.4/45631
[40] Hellman O C, Du Rivage J B and Seidman D N 2003 Efficient sampling for three-dimensional atom probe microscopy data *Ultramicroscopy* **95** 199–205
[41] Larsson A K, Haeberlein M, Lidin S and Schwarz U 1996 Single crystal structure refinement and high-pressure properties of CoSn *J. Alloys Compd.* **240** 79–84
[42] Liu M and Liu L G 1986 Compressions and phase transitions of tin of half a megabar, high temperatures *High Pressures* **18** 87–9 https://www.oldcitypublishing.com/journals/hthp-electronic-archive-home/hthp-electronic-archive-issue-contents/hthp-volume-18-number-1-1986/
[43] Dong W, Shen D, Yang S, Liang B, Wang X, Liu Y and Li S 2018 First-principles study of mechanical and electronic properties of Co–Sn intermetallics for lithium ion battery anode *Chem. Res. Chin. Univ.* **34** 235–40
[44] Kanatzidis M G, Pöttgen R and Jeitschko W 2005 The metal flux: a preparative tool for the exploration of intermetallic compounds *Angew. Chem. Int. Ed.* **44** 6996–7023
[45] Minho O, Takamatsu Y and Kajihara M 2014 Kinetics of solid-state reactive diffusion between Co and Sn *Mater. Trans.* **55** 1058–64
[46] Vassilev G P, Lilova K I and Gachon J C 2007 Calorimetric and phase diagram studies of the CoSn system *Intermetallics* **15** 1156–62
[47] Vurpillot F, Bostel A and Blavette D Trajectory overlaps and local magnification in three dimension atom probe, 200 *Appl. Phys. Lett.* **76** 3127
[48] Boll T, Al-Kassab T, Yuan Y and Liu L G 2007 Investigation of the site occupation of atoms in pure and doped TiAl/Ti_3Al intermetallic *Ultramicroscopy* **107** 796–801
[49] Boll T, Zhu Z Y, Al-Kassab T and Schwingenschlogl U 2012 Atom probe tomography simulations and density functional theory calculations of bonding energies in Cu_3Au *Microsc. Microanal.* **18** 964–70
[50] Ishida K and Nishizawa T 1991 The Co–Sn (cobalt-tin) system *J. Phase Equilib.* **12** 88–93
[51] Wang C H, Kuo C Y, Huang S E and Li P Y 2013 Temperature effects on liquid-state Sn/Co interfacial reactions *Intermetallics* **32** 57–63
[52] Kova V J, Zemanova A and Kroupa A 2019 The thermodynamic assessment of the Co–Sn system *Journal of Phase Equilibria and Diffusion* **40** 21–33
[53] Simak S I, Häußermann U, Abrikosov I A, Eriksson O, Wills J M, Lidin S and Johansson B 1997 Stability of the anomalous large-void CoSn structure *Phys. Rev. Lett.* **79** 1333–6
[54] Jang B O, Park S H and Lee W J 2013 Electrospun Co–Sn alloy/carbon nanofibers composite anode for lithium ion batteries *J. Alloys Compd.* **547** 325–30
[55] Wang C H, Huang S E and Li K T 2015 Inhibiting $CoSn_3$ growth at the Sn/Co system by minor Zn addition *Intermetallics* **56** 68–74